Source size and time dependence of multifragmentation induced by GeV ^{3}He beams

G. Wang,* K. Kwiatkowski,† D. S. Bracken,† E. Renshaw Foxford,‡ W.-c. Hsi, K. B. Morley,† V. E. Viola, and N. R. Yoder
Departments of Chemistry and Physics and IUCF, Indiana University, Bloomington, Indiana 47405

C. Volant, R. Legrain, and E. C. Pollacco
DAPNIA/SPhN, CEA/Saclay, F-91191 Gif-sur-Yvette, France

R. G. Korteling
Department of Chemistry, Simon Fraser University, Burnaby, British Columbia, Canada V5A 156

W. A. Friedman
Department of Physics, University of Wisconsin, Madison, Wisconsin 53706

A. Botvina§
INFN and Department of Physics, University of Bologna, 40126 Bologna, Italy

J. Brzychczyk
Institute of Physics, Jagiellonian University, Krakow, Poland

H. Breuer
Department of Physics, University of Maryland, College Park, Maryland 20740

To investigate the source size and time dependence of multifragmentation reactions, small- and large-angle relative velocity correlations between coincident complex fragments have been measured for the 1.8–4.8 GeV ^{3}He+ ^{nat}Ag, ^{197}Au systems. The results support an evolutionary scenario for the fragment emission process in which lighter IMFs ($Z \lesssim 6$) are emitted from a hot, more dense source prior to breakup of an expanded residue. For the most highly excited residues, for which there is a significant yield of fragments with very soft energy spectra ($E/A \lesssim 3$ MeV), comparisons with an N-body simulation suggest a breakup time of $\tau \sim 50$ fm/c for the expanded residue. Comparison of these data with both the evolutionary expanding emitting source model and the Copenhagen statistical multifragmentation model shows good agreement for heavier IMF's formed in the final breakup stage, but only the evolutionary model is successful in accounting for the lighter IMFs. [S0556-2813(99)01707-0]

PACS number(s): 25.70.Pq, 25.55.−e

I. INTRODUCTION

In order to deduce the thermodynamic properties of hot, finite nuclear matter produced in energetic nucleus-nucleus collisions, it is essential to understand the space-time evolution of the excited residues that produce the spectrum of experimental observables. A powerful tool in this regard is provided by measurements of the relative velocities between correlated fragments emitted during the breakup process [1–4]. This technique exploits the mutual Coulomb repulsion experienced by pairs of charged fragments as they emerge from the hot source to gain insight into both the source size

and emission time scale. This information serves as a vital constraint on the applicability of models proposed to explain the multifragmentation of highly excited nuclei, and ultimately, the possibility of improving our knowledge of the nuclear equation of state at low density [5–15], see also [16].

By selecting pairs of fragments emitted at large angles with respect to one another, it is possible to probe the source size at breakup. Fragment pairs originating from a nucleus at normal density and/or high temperatures should exhibit higher relative velocities than pairs from an expanded and/or cooler source. A valuable baseline for comparing the sensitivity of large-angle relative-velocity data to the Coulomb field of the multifragmenting source is provided by well-established fission total kinetic energy release (TKE) systematics [17]. Several authors have previously used the relative velocity technique in the study of both light-ion- and heavy-ion-induced reactions [1,3,18].

Relative velocity (or momentum) correlations between pairs of complex fragments emitted at small angles with respect to one another are sensitive to the emission time scale

---

[19]. Due to the Coulomb interaction, fragment pairs with small relative velocities emitted in close temporal relation to one another and along similar trajectories interact strongly. This produces a suppression of yield at small relative angles which appears as a ''Coulomb hole'' in the correlation function. This suppression disappears as the relative velocity and/or emission time difference increases. Thus, when compared with time-dependent simulations of the breakup process, the magnitude of the Coulomb suppression serves as a chronometer for the breakup time scale. Small-angle correlations have been employed by several authors to deduce time scales of order $\tau \sim 100$ fm/c for the disintegration of hot nuclei formed in heavy-ion collisions [20–24], see also [16].

In previous studies of multifragmentation induced by GeV ^{3}He ions [25,26], as well as in peripheral Au+Au collisions [27] it has been shown that excited residues with deposition energies up to $E^* \sim 1.5$ GeV are formed. For the ^{3}He beams, events exceeding the multifragmentation threshold ($E^*/A \sim 5$ MeV) have a sizable (50–100 mb) cross section [25], and there is a significant yield of sub-Coulomb-energy fragments [28–30]. These soft events are consistent with a multifragmentation mechanism that is driven by thermal expansion of a highly excited source prior to disassembly, a concept that is contained in several theoretical models of multifragmentation [5–8]. Implicit in these models is the assumption of near-simultaneous breakup for the hot residues in the final stages of expansion, as opposed to a chain of sequential evaporative emissions from a nucleus at normal density. Thus, establishing the time scale for the multifragmentation process in light-ion-induced reactions is vital to the thermal expansion scenario.

Light-ion-induced reactions offer many distinct advantages relative to heavy-ion reactions for source-size/time-scale studies via the relative-velocity-correlation technique. Most important among these is that the fragments have a unique origin; i.e., there is only a targetlike source. Further, the rapidity distributions (invariant cross sections) are nearly isotropic in the laboratory system [28], except at very forward angles. Thus, it is possible to examine the full range of emission angles, with minimal kinematic distortion of the spectra. Further advantages are suggested by intranuclear-cascade (INC) and Boltzmann-Uehling-Uhlenbeck (BUU) calculations of the collision dynamics. These indicate that energy deposition is rapid ($\tau \lesssim 30$ fm/c) [31–34], permitting an approximate decoupling of the collision and decay stages of the reaction. The calculations also predict that the residue exists in a state of depleted density and that angular momentum plays a small role ($l_{max} \lesssim 40\hbar$). Thus in principle, highly excited heavy residues produced in GeV light-ion-induced reactions are one of the most transparent experimental cases for the study of multifragmentation driven primarily by thermal forces.

In this paper we describe both small- and large-angle relative-velocity correlation analyses for data from the 1.8–4.8 GeV+ ^{nat}Ag and ^{197}Au reactions. Most of the analysis is focused on the 4.8 GeV ^{3}He+ ^{197}Au reaction, since this system yields the highest IMF multiplicities and cross sections, plus our detection energy acceptance is largest for low-energy fragments for this reaction. Estimates of the time evolution and source size characteristic of these reactions are made. These results are also compared with both the expanding emitting source (EES) model [5] and the Copenhagen statistical multifragmentation (SMM) model [6]. Abbreviated reports of these analyses have been published previously [35,36].

II. EXPERIMENTAL PROCEDURES

Measurements were performed at the Laboratoire National Saturne, using the Indiana Silicon Sphere (ISiS) 4π detector array [28–30]. Beams of 1.8, 3.6, and 4.8 GeV ^{3}He ions bombarded high purity targets of ^{nat}Ag (1.1 mg/cm^2) and ^{197}Au (1.5 mg/cm^2). Full details of the experimental apparatus are described in [30,37].

The ISiS array is a spherical structure consisting of 162 triple detector telescopes, 90 in the forward hemisphere and 72 in the backward hemisphere. It covers the polar-angle ranges from 14° to 86.5° and 93.5° to 166° and each telescope covers 20° in azimuthal angle. Each telescope consists of a gas-ionization chamber operated at ~ 17 Torr of C$_3$F$_8$, a fully depleted 500 μm ion-implanted passivated silicon detector and a 28-mm thick CsI(Tl) scintillator with photodiode readout. The telescope dynamic range permitted measurement of light-charged particles (LCP=H and He) and intermediate-mass fragments (IMF: $3 \leq Z \leq 20$) with discrete charge resolution of up to $Z \approx 20$ and energy acceptance $0.7 \leq E/A \leq 92$ MeV. Of particular relevance to this analysis is the very low energy thresholds for IMFs, which permit for the first time careful examination of the sub-Coulomb component of the multifragmentation yield. The angular resolution is relatively coarse, and hence the correlations are most sensitive for IMFs, which experience greater Coulomb deflection angles as they separate. In these experiments a multiplicity of two in the silicon detector logic was set as the minimum-bias hardware trigger.

In the analysis of the large-angle data, IMF pairs were sampled for polar angles greater than 30° and separation angles in the interval $\Psi_{rel}(1,2) = 180° \pm 40°$, where

$$\Psi_{rel}(1,2) = \arccos[\vec{v}_1 \cdot \vec{v}_2 / |v_1\|v_2|] \qquad (1)$$

and

$$v_{rel} = \vec{v}_1 + \vec{v}_2.$$

For the purposes of this analysis, IMF energy acceptance was chosen to be $0.7 \leq E/A < 10$ MeV/nucleon, corresponding to velocities in the range $2.3 \leq v_{rel} < 8.8$ cm/ns. The angular acceptance and IMF upper energy limit were chosen to minimize the contribution of nonequilibrium IMFs in this analysis [30]. This is particularly important for Li, Be, and B fragments; inclusion of the full spectrum for these elements would increase the average value of the relative velocities, $\langle v_{rel} \rangle$, especially Li.

TABLE I. Average mass values used in calculation of relative velocities. Based on Refs. [38,39].

Z	$\langle A \rangle$	Z	$\langle A \rangle$
3	6.5	9	19.49
4	8.74	10	21.58
5	10.93	11	23.72
6	12.65	12	25.70
7	14.96	13	27.96
8	17.00	14	30.81

Since only the energy and charge of each IMF were measured in these experiments, it was necessary to assume an average fragment mass in the calculation of the relative velocity. The average fragment masses used for this purpose are listed in Table I and are based on two sets of experimental data for similar systems. Each mass represents an average of those reported in Refs. [38] and [39] and the error bars indicate the upper and lower extremes of those data. We note here that the frequently used assumption $A = 2Z$, which is not consistent with experimental data, leads to higher values of $v_{\rm rel}$.

In the small-angle IMF-IMF correlation analysis, gating was performed on selected IMF kinetic energy windows and the angular range for event acceptance was again for polar angles greater than 30°. The event acceptance was restricted to the most violent events, defined by observed thermal-charged-particle multiplicities, $N_{\rm th} \geqslant 11$ [30]. This corresponded to about 7% of the measured triggers, or about 50 mb for the $^{\rm nat}$Ag target and 100 mb for ^{197}Au. Reconstruction of these events [25] indicates a range of residue excitation energies from $E^* \approx 800-1500$ MeV for ^{197}Au and $E^* \approx 500-900$ MeV for $^{\rm nat}$Ag. Two levels of cuts were imposed on the IMF kinetic energy spectra. For a global analysis, all IMFs with $(E/A)_{\rm IMF} \leqslant 10$ MeV were accepted. In addition, we have examined the behavior of the unexplored sub-Coulomb region of the spectra below $(E/A)_{\rm IMF} \leqslant 3$ MeV, which accounts for a major fraction of the spectral yield for high deposition-energy events. Because of the low velocities for these fragments, they are particularly sensitive to the Coulomb interaction between the separating fragments.

The correlation functions are calculated for a reduced velocity of the fragments,

$$v_{\rm red} = |(\vec{p}_2/m_1) - (\vec{p}_2/m_2)|/\sqrt{Z_1 + Z_2}, \qquad (2)$$

where p_i, m_i, and Z_i are the laboratory momentum, average mass, and charge of the fragments, respectively. In order to obtain maximum statistics and to normalize Coulomb effects, the factor $\sqrt{Z_1 + Z_2}$ is introduced to permit comparison of similar IMF Z values [21].

The correlation function [21] is defined as the ratio of the coincidence yield Y_{ij} for fragments with momentum p in a given event to the product of the uncorrelated yield for fragments in two separate events, $Y_{\rm mix}$, as follows:
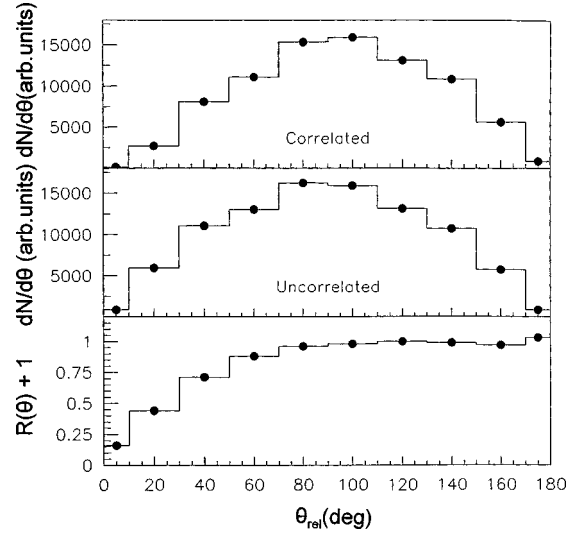

FIG. 1. Top: Number of counts of correlated IMF-IMF pairs in the 4.8 GeV ^{3}He + ^{197}Au reaction as a function of relative angle between them. Middle: Number of counts of uncorrelated IMF-IMF pairs, as above. Bottom: The ratio of correlated-to-uncorrelated pairs for this reaction.

$$R(v_{\rm red}) + 1 = C \sum_{i,j} Y_{ij}(p_i, p_j) / \sum_{(k,l)} Y_{\rm mix}(p_k, p_l). \qquad (3)$$

For both the experimental data and model calculations (Sec. IV), all correlated yields (Y_{ij}) were divided by the same number of uncorrelated fragment pairs ($Y_{\rm mix}$) in order to determine the normalization constant C. This provides a natural normalization that yields $\langle R \rangle = 0$ at large relative angles or momenta; i.e., the correlation function is unity in this case.

In Fig. 1 the behavior of Y_{ij} and $Y_{\rm mix}$ are shown as a function of relative angle $\psi_{\rm rel}$ in the upper and middle curves, respectively, for the global data set from the 4.8 GeV ^{3}He + ^{197}Au reaction. The expected peaking of these distributions near 90° due to solid angle effects is apparent. The bottom frame of Fig. 1 shows the correlation function for these data, illustrating the existence of the Coulomb suppression at small relative angles. In order to compare with the data, simulations of the correlation function were passed through the detector filter, which accounted for ISiS geometry. The effect of the filter is illustrated in Fig. 2 for a simulation with the N-body Coulomb trajectory calculation of Glasmacher [40], discussed in more detail in Sec. IV.

III. LARGE-ANGLE CORRELATION RESULTS

The relative velocity distributions for the 4.8 GeV ^{3}He reactions with $^{\rm nat}$Ag and ^{197}Au are plotted in Figs. 3 and 4, respectively. The data are plotted for IMF pairs with identical, or nearly identical charges. The uppermost curves in Figs. 3 and 4 account for event pairs for all possible charge combinations (Z_1, Z_2). Due to substantially lower cross sections for multiple IMF events in the 1.8 GeV bombardments [28], the statistics were too poor to perform the analysis at this energy.
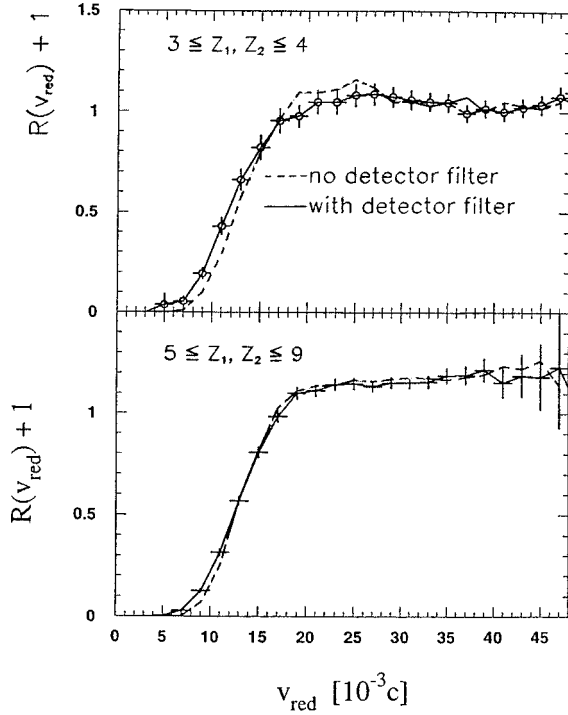
FIG. 2. Effect of detector filter on simulated events. Calculation is for the 4.8 GeV ^{3}He+^{197}Au reaction with the *N*-body code of Ref. [40], assuming a source lifetime of 50 fm/c, heaviest residue charge of $Z=12$, and fragments with energies less than 3 MeV/nucleon. Upper curve is for $Z=3,4$ IMFs and lower curve is for $Z \geqslant 5$ IMFs.

In Fig. 5 the centroids and widths of the relative velocity distributions, as defined in Eq. (1), are plotted for pairs of similar IMFs ($Z_1 = Z_2$, or for heavier fragments $Z_2 = Z_1 \pm 1$) as a function of the average IMF charge. These values
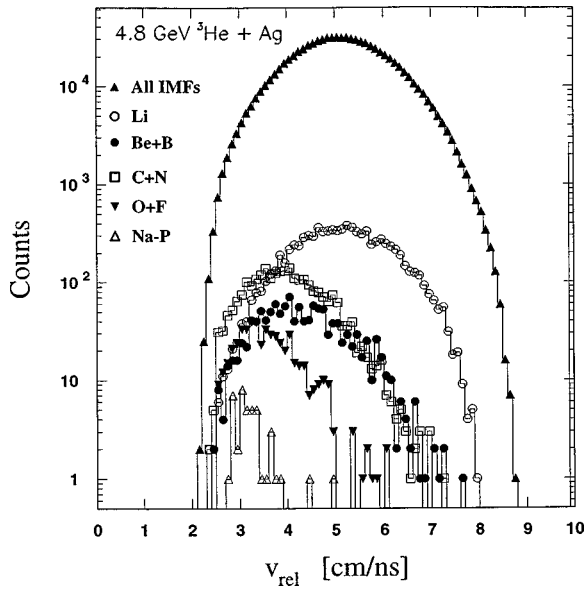

FIG. 3. Relative-velocity distributions for IMF pairs for various IMF charges, as indicated in the figure. Data are for 4.8 GeV ^{3}He +^{nat}Ag reaction.
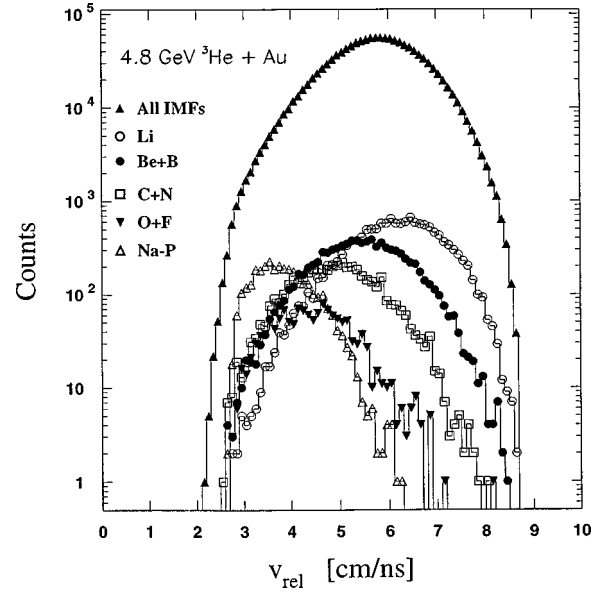

FIG. 4. Relative-velocity distributions for IMF pairs for various IMF charges, as indicated in the figure. Data are for 4.8 GeV ^{3}He +^{197}Au reaction.

are listed in Tables II and III for the ^{nat}Ag and ^{197}Au targets, respectively. The relative velocities decrease systematically as a function of IMF charge and the ^{197}Au data lie significantly above those for ^{nat}Ag, consistent with simple Coulomb-repulsion-energy expectations. The standard deviations of the v_{rel} distributions are nearly constant for IMFs up to carbon and then decrease systematically with increasing Z value. Little difference in the widths is noticed in comparing the two targets, although the ^{nat}Ag data may be reduced in part due to the fact that low-energy threshold of our detector cuts off a fraction of the IMF yield.

The centroids of the IMF v_{rel} distributions in this work are significantly higher than previously reported by Lips *et al.*
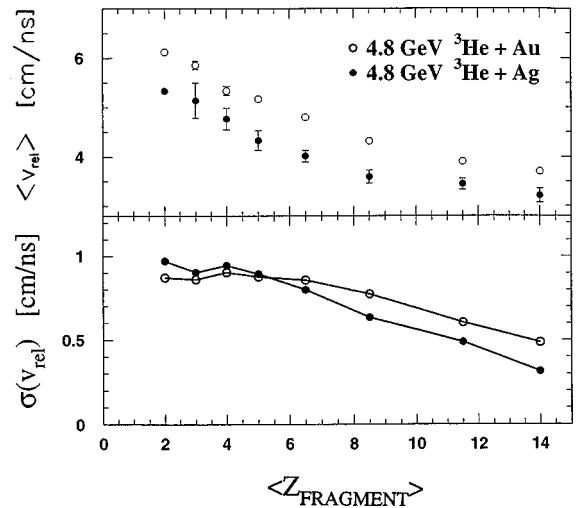

FIG. 5. Relative-velocity centroids (upper) and standard deviations (lower) as a function of the charge of the IMF pair for the 4.8 GeV ^{3}He+^{nat}Ag and ^{197}Au reactions. Higher IMF charges are binned according to Figs. 3 and 4.

TABLE II. Measured IMF average relative velocities $\langle v_{\rm rel}\rangle$ [cm/ns] and standard deviations at large relative angle for 4.8 GeV ^{3}He+Ag for different gates on IMF observed multiplicity, $N_{\rm IMF}$, and for total distribution.

$\langle Z_{\rm frag}\rangle$	$N_{\rm IMF}=2,3$		$N_{\rm IMF}=4,5$		$N_{\rm IMF}>5$		All $N_{\rm IMF}$	
	$v_{\rm rel}$	$\sigma(v_{\rm rel})$	$v_{\rm rel}$	$\sigma(v_{\rm rel})$	$v_{\rm rel}$	$\sigma(v_{\rm rel})$	$v_{\rm rel}$	$\sigma(v_{\rm rel})$
2.0	5.4	0.90	5.3	0.98	5.3	1.05	5.3	0.97
3.0	5.2	0.91	5.1	0.96	5.1	1.00	5.1	0.90
4.0	4.8	0.91	4.8	0.96	4.8	0.93	4.8	0.93
5.0	4.5	0.88	4.3	0.88	4.3	0.92	4.3	0.88
6.5	4.1	0.80	4.1	0.80	4.0	0.80	4.0	0.80
8.5	3.6	0.75	3.6	0.60	3.6	0.59	3.6	0.59
11.5	3.4	0.51	3.4	0.47	3.4	0.46	3.4	0.48
14.0	3.2	0.50	3.0	0.30	3.2	–	3.2	0.32

[41] for GeV ^{4}He-induced reactions on ^{197}Au, especially for lighter IMFs. The results of Ref. [41] have been interpreted as evidence for a breakup density of $\rho/\rho_0\sim1/7$ [18]. As will be shown below, our data require less extreme breakup densities for multifragmentation. The difference between the two experiments may be explained by the active depletion-layer thickness of the silicon detectors in the two experiments, 150 μm in [41] and 500 μm in ISiS. In the former case this corresponds to maximum fragment energies of $E/A\lesssim4$ MeV/nucleon and $v_{\rm rel}\lesssim6$ cm/ns compared with $E/A\lesssim10$ MeV/nucleon and $v_{\rm rel}\lesssim8.8$ cm/ns with the cuts imposed on the ISiS data. As can be seen in Fig. 4, a sizable fraction of the $v_{\rm rel}$ distributions would be affected by the detector cutoff in the Lips ^{4}He work.

In order to examine the effect of collision violence on the relative velocities, the $v_{\rm rel}$ centroids from the 4.8 GeV ^{3}He $+^{197}$Au reaction are shown in Fig. 6 and given in Tables II and III for three different observed multiplicity ($N_{\rm IMF}$) conditions, as indicated in the inset. For light IMFs, there is a slight decrease in $v_{\rm rel}$ with increasing $N_{\rm IMF}$; for the heaviest IMFs, the centroids for all three multiplicity bins appear to converge. The standard deviations of the light IMF distributions in Tables II and III also appear to increase for higher $N_{\rm IMF}$ values, whereas they are nearly independent of $N_{\rm IMF}$.

TABLE III. Measured IMF average relative velocities $\langle v_{\rm rel}\rangle$ [cm/ns] and standard deviations at large relative angle for 4.8 GeV ^{3}He+Au for different gates on IMF observed multiplicity, $N_{\rm IMF}$, and for total distribution.

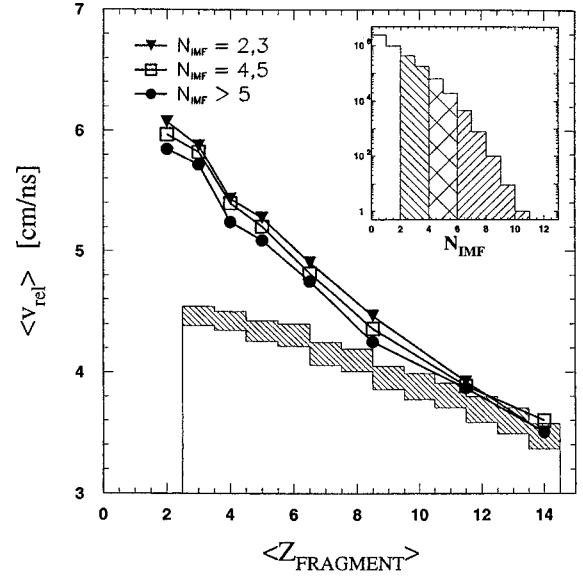| $\langle Z_{\rm frag}\rangle$	$N_{\rm IMF}=2,3$		$N_{\rm IMF}=4,5$		$N_{\rm IMF}>5$		All $N_{\rm IMF}$	
	$v_{\rm rel}$	$\sigma(v_{\rm rel})$	$v_{\rm rel}$	$\sigma(v_{\rm rel})$	$v_{\rm rel}$	$\sigma(v_{\rm rel})$	$v_{\rm rel}$	$\sigma(v_{\rm rel})$
2.0	6.1	0.77	6.0	0.82	5.8	0.93	6.1	0.88
3.0	5.9	0.79	5.8	0.81	5.7	0.89	5.9	0.87
4.0	5.0	0.81	5.4	0.83	5.2	0.94	5.3	0.90
5.0	5.3	0.84	5.2	0.84	5.1	0.89	5.2	0.88
6.5	4.9	0.80	4.8	0.82	4.7	0.87	4.8	0.87
8.5	4.5	0.74	4.4	0.77	4.3	0.77	4.3	0.78
11.5	3.9	0.61	3.9	0.59	3.9	0.61	3.9	0.60
14.0	3.5	0.60	3.6	0.49	3.5	4.9	3.7	0.50

FIG. 6. Average relative-velocity centroids for fragment pairs corresponding to Fig. 3 and separation angle $\Psi_{\rm rel}=180°\pm40°$, for the 4.8 GeV ^{3}He+^{197}Au reaction, gated on IMF multiplicity. Shaded area gives expected average velocity centroids for fission TKE systematics, as described in text. Insert indicates distribution of IMF multiplicities with the gates highlighted.

for $Z\gtrsim8$ fragments. This result suggests that a broader distribution of source conditions may be responsible for producing the lighter IMFs.

In order to provide a baseline for comparing the sensitivity of the $v_{\rm rel}$ data to the Coulomb field of the emitting source, the centroids are also compared with values based on fission kinetic- energy-release (TKE) systematics [17] in Fig. 6. The fission estimates assume two successive fission steps from the postcascade targetlike residue. The Z and A of the fissioning source are estimated from well-tested INC calculations [42], which are in agreement with source reconstruction calculations for these experimental data [25]. These predict a range of residue nuclides for the 4.8 GeV ^{3}He $+^{197}$Au system between $Z=72$, $A=179$, and $Z=65$, $A=165$ for deposition of excitation energies between 5 to 10 MeV per residue nucleon, respectively. This range is accounted for by the shaded region in Fig. 6. For nuclei in this mass range, fission TKE systematics yield a radius parameter $r_0\cong1.8$ fm for the effective charge-separation distance at scission, $d=r_0(A_1^{1/3}+A_2^{1/3})$. Compared to a value of $r_0=1.2$–1.4 fm for nuclei at normal density, this would correspond to a density of $\rho/\rho_0\approx0.3$–0.5 if the separation were radial instead of axial. The effect of the source temperature on $v_{\rm rel}$ has also been included in the fission calculations, assuming a temperature of 5 MeV. As shown in Fig. 7, the largest effect of source temperature is on the lightest IMFs, which improves the agreement with the slope of the data. However, the Li-B fragments are still underpredicted by a large amount. These same results are obtained for the $^{\rm nat}$Ag target.

The most prominent feature of Figs. 6 and 7 is that even for the most violent events, the experimental centroids for the lighter IMFs lie well above the simple Coulomb-
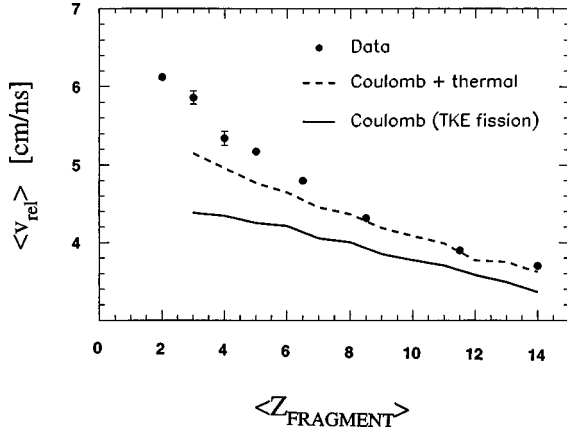
FIG. 7. Comparison of data in Fig. 5 for fission source at $T = 0$ (solid curve) and $T = 5$ MeV (dashed curve).

repulsion predictions of fission systematics. This picture does not change appreciably if additional centrality cuts are imposed on the data, or if the calculated v_{rel} values are supplemented by a thermal source with $T = 5$ MeV. This suggests that on average, light IMFs have their origin in more dense and/or hotter sources of higher charge than heavier IMFs. This perhaps reflects an expansion boost or coalescence-like processes associated with secondary scatterings during the latter stages of the cascade but prior to maximum expansion/dilution of the source.

In contrast, for the heaviest IMFs ($Z \gtrsim 8$), there is good overall agreement with the fission systematics. The corresponding radius parameter is consistent with emission from an expanded/dilute source with $\rho < \rho_0/2$. Thus, these results are consistent with a time-dependent picture of multifragmentation in which light IMFs are emitted from a hot, expanding source, followed by breakup of a dilute residue in which IMFs of all charges are emitted.

In Fig. 8, the average relative velocity centroids for all N_{IMF} bins (Fig. 5) are compared with predictions of two hybrid models. For both model calculations, identical INC calculations [42] provided the distribution of residue mass, charge, and excitation energy produced in the fast cascade
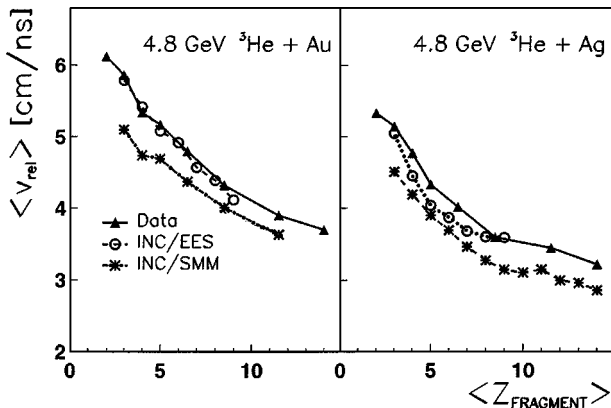
phase of the reaction. This distribution then served as input for the time-dependent expanding evaporating source (EES) [5] and simultaneous (multifragmentation SMM) [6] models. The default conditions of both models, which have been successful in fitting heavy-ion multifragmentation data [16], have been employed. For comparison with the data, energy thresholds were imposed on both calculations to conform to the ISiS detector acceptance and software cuts ($2.3 \leq v_{rel} \leq 8.8$ cm/ns).

The EES and SMM models provide quite different perspectives on the time evolution of the disassembly process. The EES model invokes a time-dependent scenario for IMF emission, assuming isentropic monopole oscillations of a hot source that emits primarily light fragments (surface emission) as it expands and cools [5]. For sufficiently high temperatures, the amplitude of the initial oscillation exceeds the cohesive nuclear forces, leading to breakup on a time scale of order 100 fm/c. At this stage volume emission is assumed and heavy fragment production becomes strongly favored.

In the INC/EES calculation, the effective compressibility parameter is $K = 144$ MeV, for which $\rho \sim \rho_0/3$ at breakup [43]. This value of K is comparable to that estimated for a finite-charged nucleus relative to standard nuclear matter [44]. The model of Ref. [43] has been previously shown to account for the IMF multiplicities and energy spectra in the 4.8 GeV ^{3}He + ^{197}Au, ^{nat}Ag reactions [28,29].

The SMM model [6] assumes instantaneous statistical decay of a hot expanded residue into many fragments. In the version of the model employed in these comparisons, a freeze-out volume is assumed in which the fragments attain full statistical equilibrium (maximum entropy). The default value of the critical radius corresponding to $\rho_0/3$ is employed here. No preequilibrium stage is included between the fast cascade and breakup steps in either of these calculations.

A similar comparison can be made using the code SIMON [45,46] for which we have put the same angular and energy conditions as on the data. Two options were examined: (1) evaporation, or sequential IMF emission, and (2) explosion, or simultaneous disassembly. The Coulomb trajectories are calculated, the thermal motion is taken into account, and the formed fragments are allowed to decay. For the first option, a full calculation has been done using INC code [47] outputs to feed into the evaporation code, which then computes the decay of a residue at normal density. Comparisons are shown by the triangles in Fig. 9, where the data are plotted as a function of the sum of the IMF charges. The results are similar to the empirical fission calculations. The calculated widths are found to decrease only slightly with increasing charge sum (σ from 1.0 to 0.8 cm/ns, similar to the results in Fig. 5). Another calculation, which assumes an average source with a given E^*/A of 5 MeV and a laboratory velocity of 0.01c, consistent with the rapidity analysis [28] and average mass and charge taken from INC, shows similar results. This last source has also been used for the explosion option where three fragments are assumed randomly distributed in space inside a sphere of maximum compactness but with a constraint of a minimal distance of 2 fm between the fragment surfaces.
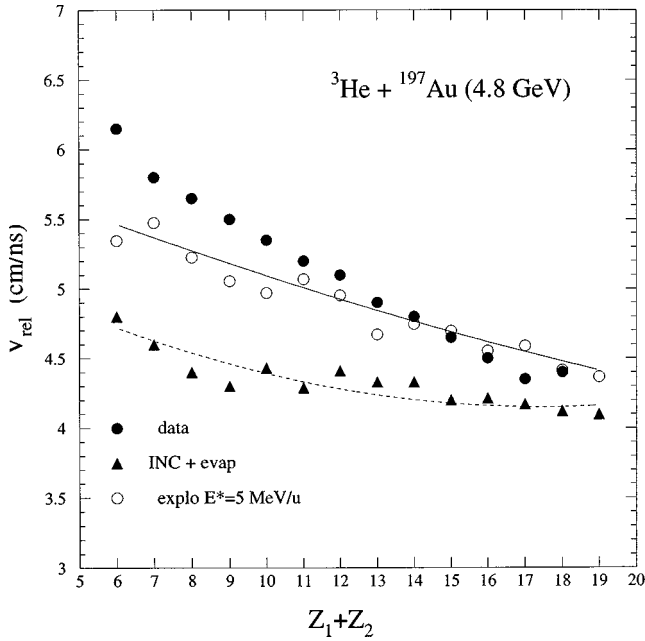

FIG. 8. Comparison of relative-velocity centroids for the ^{nat}Ag and ^{197}Au targets with predictions of two hybrid calculations, INC/EES and INC/SMM, as described in the text.

FIG. 9. Comparison of relative-velocity centroids (●) for the ^{197}Au target with predictions of the model of Durand [44], assuming a source temperature of $E^*/A = 5$ MeV and two breakup scenarios: INC and evaporation (△) and explosion (○). Dashed and solid curves show mean trends of the calculations.

The comparison is shown in Fig. 9 for the 4.8 GeV ^{3}He $+ ^{197}$Au reaction. The results parallel those of the INC/SMM calculation and fission systematics. The INC plus evaporation option fails to reproduce both the relative velocities and their slope as a function of charge. The explosion option with $E^*/A = 5$ MeV accounts for the higher Z fragments, but again fails to describe the slope. Similar trends are observed for silver.

In comparing with the data, the most sensitive test of the models is their ability to account for both the absolute values and the slope/curvature of the v_{rel} vs Z dependence. The absolute magnitude of the results can be altered by adjusting the radius parameter r_0, but this has minimal effect on the curvature. In Fig. 8, the INC/EES simulation is found to be in general agreement with the v_{rel} data for ^{197}Au, both in absolute magnitude and the curvature of the Z dependence. For the ^{nat}Ag target the agreement is somewhat poorer. The agreement is less satisfactory for the INC/SMM and Durand cases, although for the heaviest fragments ($Z \gtrsim 8$), the concordance with the data is reasonable.

In Fig. 10, the model dependence on source density is examined. In the lower frame, the schematic INC/EES model is compared with the ^{197}Au data for two cases, $K = 144$ MeV (expansion) and $K = \infty$ (no expansion). The latter case corresponds to emission from a static source at normal nuclear matter density. The similarity in light IMF v_{rel} values for both assumed values of K reflects the similar probability for fragments to be emitted early in the deexcitation process from a higher-Z source closer to normal density. In addition, the Li fragments from the $K = 144$ MeV calculation may exhibit some velocity enhancement due to the expansion boost. As the fragment charge increases, the calcu-
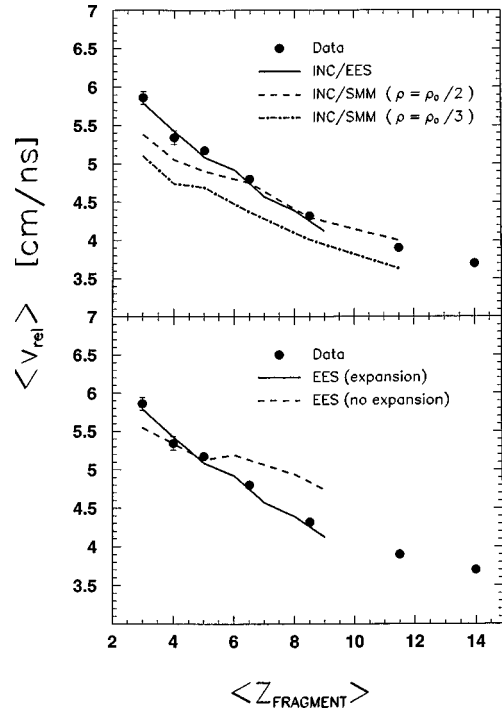

FIG. 10. Upper: Average relative velocity for fragment pairs for 4.8 GeV ^{3}He $+ ^{197}$Au reaction. Predictions of the INC/EES calculation are given by solid line and INC/SMM predictions by dot-dashed lines ($\rho = \rho_0/3$) and dashed line ($\rho = \rho_0/2$). Lower: Average reduced velocity for centroid fragment pairs. Comparison is with INC/EES model for two conditions: $K = 144$ MeV (solid line, corresponding to expansion) and $K = \infty$ (dashed line, corresponding to emission from a system at normal nuclear matter density).

lation clearly shows a significant increase in the relative velocity centroids from the stiffer, more compact source.

As shown in the upper frame of Fig. 10 an increase in the freeze-out density in the SMM calculation to $\rho = \rho_0/2$ would bring the simulation in line with the data for the heavier IMFs. However, this adjustment would not affect the slope/curvature and thus would still significantly underpredict the v_{rel} centroids for the lighter IMFs.

The larger predicted average relative velocities for the low-Z fragments for the INC/EES calculation relative to those for INC/SMM is consistent with the emission of IMFs early in the expansion phase of the highly excited residues. During this period, the source density is higher, as are both the source charge and temperature, thus producing more energetic fragments. In addition, the early (light) fragments may receive an expansion boost [5]. This pre-breakup IMF emission stage, in which ejectiles with $Z \lesssim 6$ are preferentially emitted, bridges the interval between the fast cascade and multifragment breakup. It is an aspect of the disassembly mechanism that is present in the EES but not in the SMM and SIMON codes used here. While a preequilibrium option can be implemented preceding the SMM stage in the code of [6], it allows only for H and He emission and hence would affect the present results only by cooling the source and reducing the charge of the residue. This argues for the inclusion of some form of IMF precursor stage in comparing the statistical model calculations with data. Nonetheless, com-
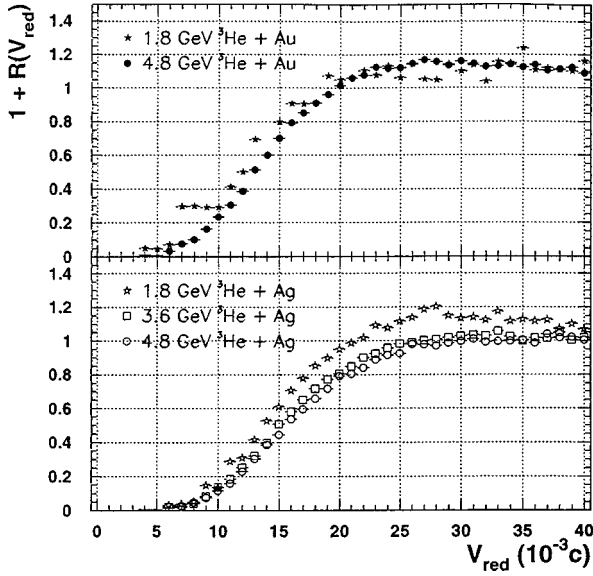
FIG. 11. Bombarding energy dependence of the reduced-velocity correlation functions. Top: the ^{3}He$+^{197}$Au reaction, and bottom: the ^{3}He$+^{nat}$Ag reaction. All IMF multiplicities with $N_{IMF} \geqslant 2$ and fragment kinetic energies between $0.7 \leqslant E_{IMF}/A \leqslant 10$ MeV are indicated in the data set.

FIG. 12. Target dependence of the reduced-velocity correlation functions shown in Fig. 10.

parisons of the data with all three calculations are consistent with a time-dependent model in which the final breakup occurs from a system at low density.

IV. SMALL-ANGLE CORRELATIONS

While the large-angle-correlation analysis in Sec. III is consistent with a time-dependent scenario in which IMF emission occurs from an expanding source, the time-scale for the final breakup is critical in differentiating between a sequential or instantaneous mechanism. Information relevant to this issue can be deduced from comparison of measured small-angle reduced-velocity correlations with time-dependent model simulations [19]. This approach has been followed in numerous heavy-ion studies, yielding a range of relative emission times between $\tau \sim 1000$ fm/c for evaporationlike phenomena [1] to $\tau \sim 100$ fm/c for high multiplicity events in intermediate energy heavy-ion reactions [21–24]. In this section we present the results of similar investigations for GeV light-ion induced reactions. Of particular interest in this analysis is the time scale for that portion of the IMF kinetic energy spectrum that is characterized by sub-Coulomb fragment energies. These fragments provided the earliest suggestion of expansion [48,49] in GeV proton-induced reactions and have subsequently been shown to be associated with the most violent collisions in light-ion induced reactons [28,29,50]. Because of their very low energies, these events may constitute one of the best experimental cases for studying multifragmentation driven primarily by thermal forces.

In Fig. 11 the reduced-velocity correlation function [Eq. (3)] is plotted for all multiplicities $N(_{IMF} \geqslant 2)$ for the five systems studied in this work. The supression of correlated events at low reduced velocity is seen to grow as a function
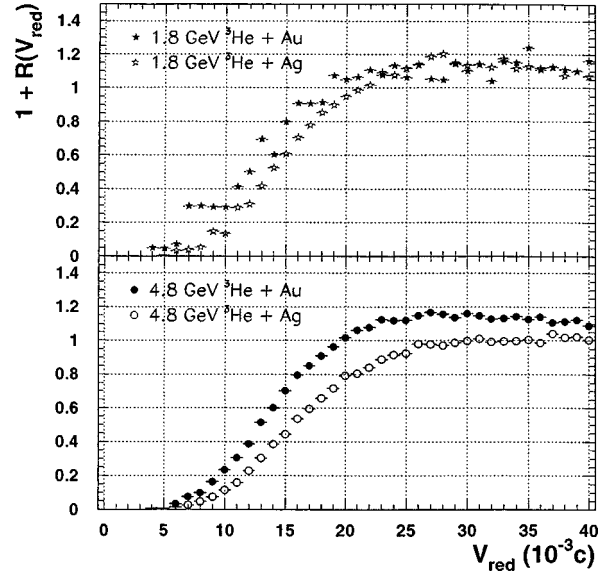
of bombarding energy in each case, suggesting somewhat shorter time scales for reactions induced by the more energetic projectile. Figure 12 shows the same results, comparing instead the target mass. At each energy, the ^{nat}Ag target yields the largest supression, consistent with the smaller breakup volume and lower IMF velocities for this system.

Of more direct concern is the dependence of the v_{rel} correlation function on collision violence. Here we have chosen the number of thermal charged particles, which is directly proportional to the deposition energy [30], as our gauge of deposition energy. It is observed in Fig. 13 that as the number of thermal charged particles increases, the supression at
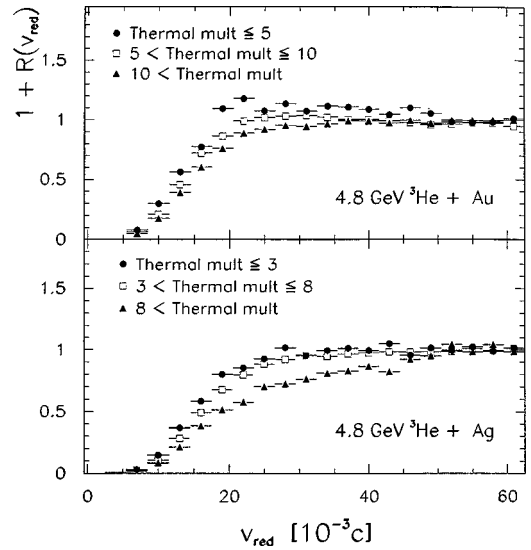

FIG. 13. Dependence of reduced-velocity correlation function on the multiplicity of thermal charged particles for the 4.8 GeV ^{3}He$+^{197}$Au (upper) and ^{nat}Ag (lower) reactions. Acceptance of IMF pairs is the same as in Fig. 11. Multiplicity gates are indicated on figure.

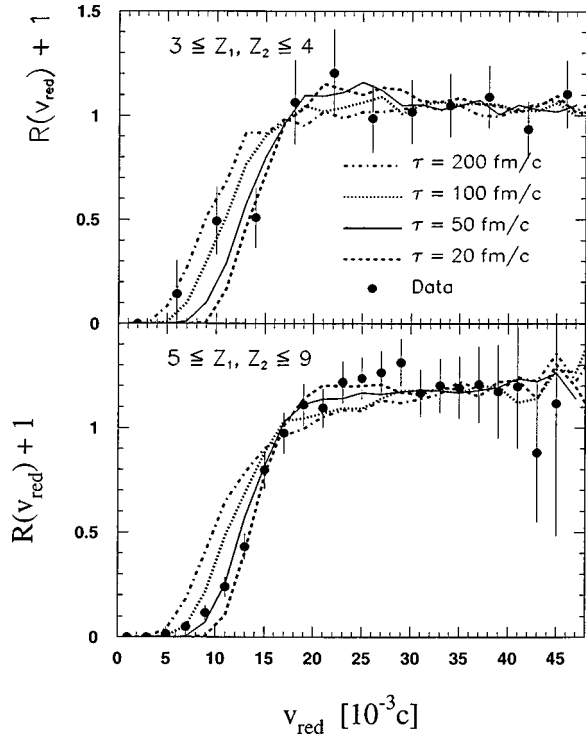FIG. 14. Reduced-velocity correlations as a function of reduced velocity for the 4.8 GeV ^{3}He$+$^{197}Au reaction (points). Data were selected for pairs of events in which $N_{th} \lesssim 11$ and $(E/A)_{IMF} = 0.7$–3.0 MeV and are shown for $Z=3,4$ fragments (upper frame) and $Z=5$–9 fragments (lower frame). Lines are results of an N-body simulation with $\rho/\rho_0 = 0.25$ and maximum residue size, $Z_{res}=12$. Time scales are indicated in the figure.

low v_{red} grows substantially, suggesting a shorter time scale.

To investigate this effect further, we have examined the reduced-velocity correlation function for those low-energy IMFs associated with the most violent events ($E_{IMF}/A \lesssim 3$ MeV/nucleon and thermal multiplicity $M_{th}>11$). The experimental correlation functions are plotted in Fig. 14 for two IMF conditions: light fragments ($Z=3$–4) and heavy fragments ($Z=5$–9). This separation was imposed to isolate nonequilibrium contributions to the spectra, as discussed in the previous section. The significant Coulomb suppression at low relative velocity is apparent in the data.

In order to estimate the breakup time scale, the correlation-function results are compared with the N-body Coulomb trajectory calculation of Glasmacher *et al.* [40], which has been run through the ISiS software acceptance filter. In this code, the relative time interval between fragments is sampled assuming the relation e^{-t/τ_0}, where τ_0 is the source lifetime. Fragments are randomly selected according to the experimental multiplicity and charge distributions. The latter are shown in the upper frame of Fig. 15. It is observed that the charge distribution for soft events is significantly flatter than that for higher energies; the former corresponding to a power-law exponent $\tau_z \approx 1.7$ and the latter to a value of $\tau_z \cong 3.1$. Both distributions are described better with an exponential function of the form
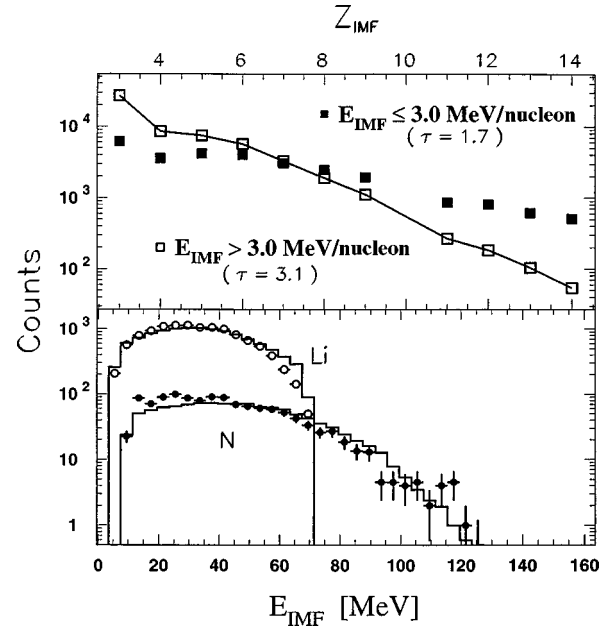
$$\sigma(Z) \propto e^{-aZ},$$

FIG. 15. Upper frame: Relative charge distributions for events with $(E/A)_{IMF}>3.0$ MeV (open squares) and $(E/A)_{IMF}<3.0$ MeV (closed squares) for 4.8 GeV$+$^{197}Au reaction. Lines are to guide the eye. Lower frame: Energy spectra of Li and N fragments (open and closed points, respectively). Solid lines are output from N-body simulation.

where $a=0.25$ in the former case and $a=0.60$ in the latter. With the exponential function, χ^2 values were about a factor of three lower.

In the analysis, we employ source velocity and Coulomb-barrier parameters derived from moving-source fits to the experimental energy spectra [30,51], corresponding to the event energy and multiplicity gates. In this procedure, the Coulomb-barrier function in the spectral parametrization is effectively subtracted from the moving-source fits in the input step. This raw thermal spectrum in the source frame is then boosted back in when performing the N-body Coulomb-trajectory calculation. The output of the simulation is required to match the experimental kinetic energy spectra for these thermal-like events, examples of which are shown in the bottom frame of Fig. 15 for a breakup time of 50 fm/c. The spectral shape of the simulation is quite sensitive to the input parameters; thus, the small deviations for nitrogen fragments below $E/A_{IMF} \lesssim 1$ MeV represent good fits.

Three features of the simulation were important in obtaining a simultaneous fit to both the spectra and the relative velocity correlations. First, it was necessary to employ a breakup density significantly lower than normal; in these calculations we use $\rho/\rho_0 = 0.25$, consistent with earlier results [43] and those presented in Sec. III, as well as theoretical models [5,6,8]. Second, the location of the heaviest residue in the N-body ensemble had to be randomly placed within the breakup volume (rather than a fixed central position). Finally, the fragment with the largest charge in the N-body ensemble needed to be small to reproduce the shape. The calculations shown in Fig. 14 used a value of $Z_{res}=12$ for the charge of the largest residue, although the range of Z_{res}
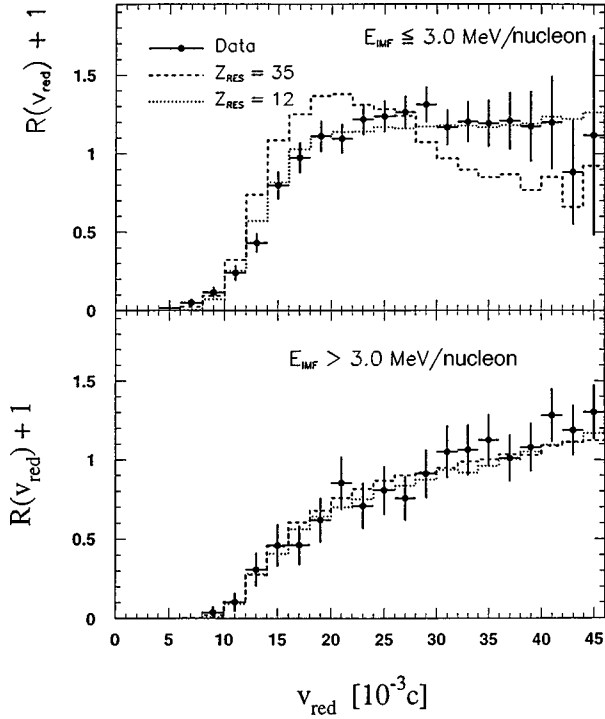
FIG. 16. Comparison of experimental reduced-velocity correlations for $5 \leqslant Z_1, Z_2 \leqslant 9$ for 4.8 GeV ^{3}He+^{197}Au reaction with *N*-body simulation for maximum residue size $Z = 12$ and 35, as indicated in the figure. Time is 50 fm/c in each case. Upper frame is for $(E/A)_{\mathrm{IMF}} \leqslant 3.0$ MeV fragments and lower frame for $(E/A)_{\mathrm{IMF}} > 3.0$ MeV.

≈ 10–20 is within the error limits. This compares with the average charge of $Z_{\mathrm{res}} \sim 25$ determined independently from reconstructed events with a similar centrality cut [25]. The requirement of both a short time scale and small size of the largest residue in order to fit both the correlation functions and the energy spectra imposes a significant constraint on the ambiguities in these parameters.

The residue size effect is important only for the soft component of the IMF spectra, as illustrated in Fig. 16. Here the experimental correlation function for $Z = 5$–9 fragments is compared with the *N*-body calculation for maximum residue sizes $Z_{\mathrm{res}} = 12$ and 35; in each case the breakup time is 50 fm/c. For the $(E/A)_{\mathrm{IMF}} > 3.0$ MeV fragments (bottom frame), there is little sensitivity to the maximum remnant size. Time scales of $\tau_0 \sim 50$–100 fm/c describe this component well, comparable to an earlier ^{4}He study [52] and to heavy-ion results [21,22,24] for this fragment energy domain.

The *N*-body Coulomb trajectory simulations are compared with the ^{197}Au data in Fig. 14 for breakup times of $\tau_0 = 20$, 50, 100, and 200 fm/c. For the $Z = 5$–9 fragments, a value of $\tau_0 \simeq 50$ fm/c describes the data well. In this regard it should be noted that these time scales are based on the same simulations that yield breakup time scales of $\tau \lesssim 50$–100 fm/c in heavy-ion reactions [40]. This analysis supports a picture in which the low-energy debris formed in the reaction originates in high deposition-energy processes in which clusterization of the system occurs from an expanded/

dilute source on a near-instantaneous time scale. The extracted time scales are consistent with instantaneous models of multifragmentation [6–8]. They are also in accord with the time-dependent model of Ref. [5], for which 80% of the fragments with kinetic energies $E/A < 7$ MeV are predicted to be emitted within 70 fm/c.

The short mean lifetimes implied by the analysis here are comparable to the reaction relaxation time for these collisions predicted by Boltzmann-Uehling-Uhlenbeck calculations [31], $\tau_R \sim 30$–40 fm/c. This value is also near the characteristic time for thermodynamic fluctuations for a source at temperature $T = 4$–6 MeV [26,27]; i.e., $\tau_{\mathrm{fluc}} \approx \hbar/T = 30$–50 fm/$c$ [53,54]. This suggests that dynamical fluctuations — perhaps surviving from the fast collision stage — may play an important role in the disassembly process.

For the lighter ($Z = 3,4$) IMFs, the breakup time is more poorly defined. Because the population of events with sub-Coulomb energies is significantly reduced for these fragments relative to heavier IMFs (Fig. 15), the statistical sample is much smaller ($\sim 20\%$). This is also reflected by the relative velocity distributions for Li and B in Fig. 3. Extension of the upper energy acceptance to $(E/A)_{\mathrm{IMF}} \leqslant 4.0$ MeV removes most of the fluctuations in the $Z = 3,4$ data in Fig. 14, but does not alter the average trend. Taken at face value, the correlation-function data suggest that light fragments are associated with a convolution of emission times, ranging from $\tau_0 = 20$–200 fm/c. This implies that significant yields of these light IMFs may originate via multiple mechanisms, extending from the pre-breakup stage prior to or during expansion, to the final multifragment disassembly. This conclusion is consistent with a time-dependent disassembly picture deduced from large-angle IMF-IMF correlations discussed in Sec. III.

The reduced-velocity correlation functions, comparable to Fig. 14, for the 4.8 GeV ^{3}He+$^{\mathrm{nat}}$Ag system are shown in Fig. 17. Because of the lower average energies for fragments from the $^{\mathrm{nat}}$Ag target and the fact that a substantial fraction of events occur below the low-energy detector threshold, no fragment kinetic energy condition has been set on the data. Thus, the fits in this case are much less conclusive, yielding time scales in the range $\tau \approx 50$–200 fm/c. We attribute this result as possible evidence that the smaller size and higher average excitation energy [25] lead to enhanced fragment emission prior to final breakup of the hot source.

In Fig. 18 the reduced-velocity correlations for the thermal-like IMFs with $M_{\mathrm{th}} \geqslant 11$, including all fragment energies up to 10 MeV, are shown along with predictions of the INC/SMM model [7], passed through the detector filter. The SMM calculation again assumed the default parameters, as discussed in Sec. III. Two excitation-energy assumptions for the SMM calculation are shown: $E^*/A = 5.3$ and 7.7 MeV and results are shown for both light and heavy IMFs. For the $Z = 5$–9 fragments, good agreement is found for the $E^*/A = 7.7$ MeV case. On the other hand, the $Z = 3$–4 fragment pairs are described poorly at low relative velocities. Increasing the SMM breakup density to normal density improves the fit somewhat, but still leaves a strong disagreement with the data at low reduced velocities. This effect is due in part
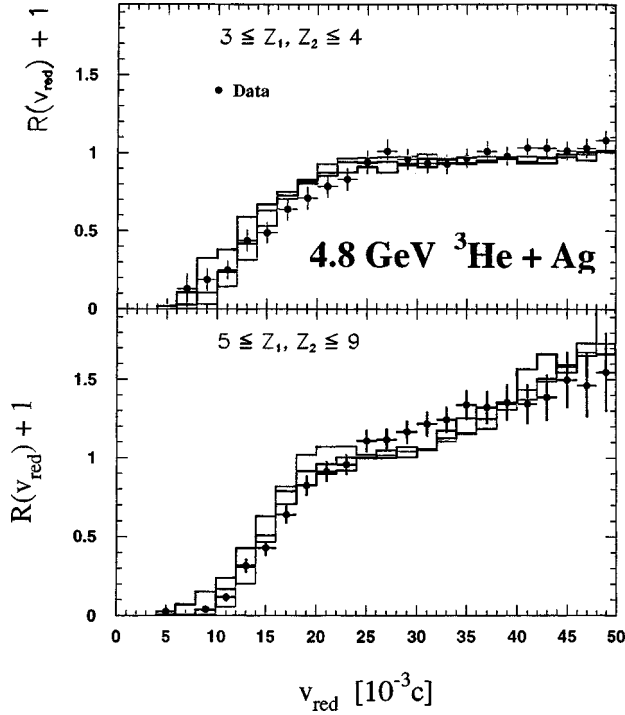
FIG. 17. Reduced-velocity correlation function for the 4.8 GeV ^{3}He$+^{nat}$Ag reaction, as in Fig. 12, except that all IMFs with $E_{IMF}/A \lesssim 10$ MeV are included in the data set and $N_{th} \geqslant 8$. Histograms are for $\tau = 50$, 100, and 200 fm/c; solid points are data.
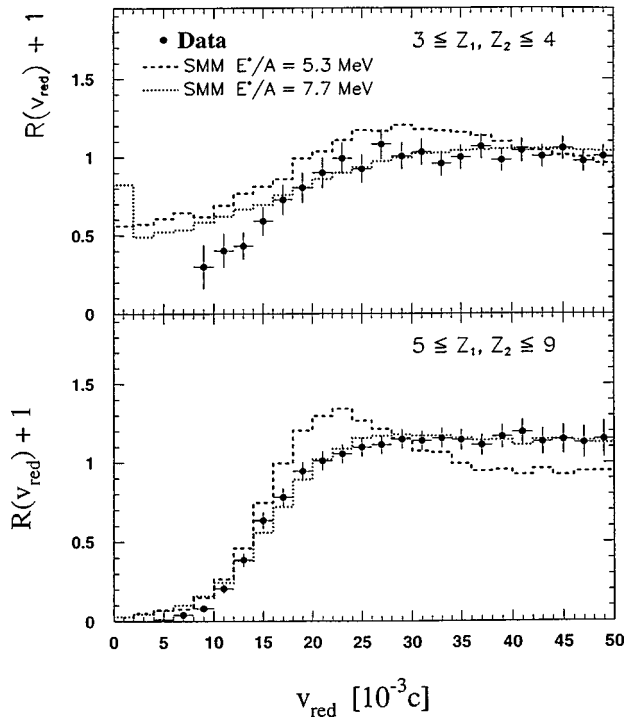

FIG. 18. Comparison of reduced-velocity correlations for $(E/A)_{IMF} < 10$ MeV with predictions of SMM model at $E^*/A = 5.3$ and 7.7 MeV, as indicated on figure, for 4.8 GeV ^{3}He $+^{197}$Au reaction. Upper frame is for $Z = 3,4$ fragments and lower frame for $Z = 5-9$ fragments.

to the Fermi breakup mechanism employed in the postacceleration stage of the SMM code to account for deexcitation of the hot primary fragments. This decay mechanism produces significant yields of secondary Li fragments that can randomly correlate with primary Li ions.

V. CONCLUSIONS

The composite picture that emerges from these IMF-IMF correlation studies of GeV light-ion-induced reactions is as follows. The data suggest that for the most highly excited residues, fragmentation is a time-dependent phenomenon in which light IMFs are emitted preferentially from a hot, expanding source followed by a near-simultaneous breakup that is primarily responsible for heavier fragments. Comparisons of the large-angle-correlation data with hybrid-model INC/EES and INC/SMM calculations satisfactorily account for the heaviest IMFs. However, the time-dependent EES model describes the relative velocities for light fragments and the overall slope of the data better. This result points to the need to complement IMF formation in instantaneous statistical models with a pre-breakup mechanism to account for emission during the late stages of the cascade, prior to breakup of the dilute residue.

Breakup times of the order of $\tau \lesssim 100$ fm/c are indicated by small-angle reduced-velocity correlations between IMF pairs. However, this time scale is dependent on collision violence, shorter times being associated with more violent collisions, as reflected by IMF and thermal charged-particle multiplicities. For this reason the soft, sub-Coulomb component of the spectrum has been investigated for the first time. Comparisons with an N-body Coulomb-trajectory simulation indicate rapid breakup of these highly excited, thermal-like residues, with a mean disassembly time of $\tau_0 \approx 50$ fm/c for the heavier clusters $(Z = 5-9)$. This time is short relative to the thermodynamic relaxation time and suggests that quantal/dynamical fluctuations may play an important role in the disassembly process. In order to fit the experimental spectra and relative-velocity correlation functions simultaneously, the simulation requires a breakup density of $\rho/\rho_0 \sim 1/4 - 1/3$, average heavy remnant size of $Z_{res} \sim 10 - 20$, and the random placement of the heaviest remnant in the breakup volume. For lighter IMFs, the time scale is more poorly defined, suggesting an evolutionary process in which multiple sources produce these fragments. Comparison with SMM calculations agrees well with the data for heavier IMFs emitted from a source at $E^*/A = 7.7$ MeV.

In summary, the implication of these results is that multifragmentation studies with GeV light ions may provide one of our most transparent examples for learning the thermal properties of finite nuclear matter at high excitation energies.

[1] R. Tröckel *et al.*, Phys. Rev. Lett. **59**, 2844 (1987).

[2] J. Randrup and J. Lopez, Nucl. Phys. **A491**, 477 (1989).

[3] G. Klotz-Engmann *et al.*, Nucl. Phys. **A499**, 392 (1989).

[4] J. Pochodzalla *et al.*, Phys. Lett. B **232**, 41 (1989).

[5] W. A. Friedman, Phys. Rev. C **42**, 667 (1990).

[6] A. Botvina, A. S. Iljinov, and I. Mishustin, Nucl. Phys. **A507**, 649 (1990).

[7] J. P. Bondorf, A. S. Botvina, A. S. Iljinov, I. N. Mishustin, and K. Sneppen, Phys. Rep. **257**, 133 (1995).

[8] D. H. E. Gross, Rep. Prog. Phys. **53**, 605 (1990).

[9] J. Randrup and S. E. Koonin, Nucl. Phys. **A356**, 223 (1981).

[10] J. Aichelin, J. Hüfner, and R. Ibarra, Phys. Rev. C **30**, 107 (1984).

[11] J. Aichelin, Phys. Rep. **202**, 233 (1991).

[12] G. F. Bertsch and S. Das Gupta, Phys. Rep. **160**, 189 (1988).

[13] L. Vinet, C. Grégoire, P. Schuck, B. Remaud, and F. Sébille, Nucl. Phys. **A468**, 321 (1987).

[14] S. Koonin and J. Randrup, Nucl. Phys. **A474**, 173 (1987).

[15] A. Ono, H. Horiuchi, T. Arayama, and A. Ohniski, Prog. Theor. Phys. **87**, 1185 (1985).

[16] W. G. Lynch, Rev. Mod. Phys. (to be published).

[17] V. E. Viola, K. Kwiatkowski, and M. Walker, Phys. Rev. C **31**, 1550 (1985).

[18] B.-An Li *et al.*, Phys. Lett. B **335**, 1 (1994).

[19] W. Bauer, C. K. Gelbke, and S. Pratt, Annu. Rev. Nucl. Part. Sci. **42**, 77 (1992).

[20] R. Bougault, J. Colin, F. Dulaunay, A. Genoux-Lubain, A. Hajfani, C. LeBrun, J. F. Lecolley, M. Louvel, and J. C. Stekmeyer, Phys. Lett. B **232**, 291 (1989).

[21] Y. D. Kim *et al.*, Phys. Rev. Lett. **67**, 14 (1991); Phys. Rev. C **45**, 387 (1992).

[22] D. R. Bowman *et al.*, Phys. Rev. C **52**, 818 (1995).

[23] C. Gelderloos and J. M. Alexander, Nucl. Instrum. Methods Phys. Res. A **349**, 618 (1994); C. Gelderloos *et al.*, Phys. Rev. Lett. **75**, 3082 (1995).

[24] D. Fox *et al.*, Phys. Rev. C **47**, R421 (1993).

[25] K. Kwiatkowski *et al.*, Phys. Lett. B **423**, 21 (1998).

[26] K. Kwiatkowski *et al.*, in *Advances in Nuclear Dynamics 4*, edited by W. Bauer (Plenum, New York, 1998), p. 173.

[27] J. Pochodzalla *et al.*, Phys. Rev. Lett. **75**, 1040 (1995).

[28] E. Renshaw Foxford *et al.*, Phys. Rev. C **54**, 749 (1996).

[29] K. Kwiatkowski *et al.*, Phys. Rev. Lett. **74**, 3756 (1995).

[30] K. B. Morley *et al.*, Phys. Lett. B **355**, 52 (1995); Phys. Rev. C **54**, 737 (1996).

[31] G. Wang, K. Kwiatkowski, V. E. Viola, W. Bauer, and P. Danielewicz, Phys. Rev. C **53**, 1811 (1996).

[32] J. Cugnon, Nucl. Phys. **A462**, 751 (1987).

[33] W. Bauer, G. F. Bertsch, W. Cassing, and U. Mosel, Phys. Rev. C **34**, 2127 (1986).

[34] P. Danielewicz and G. F. Bertsch, Nucl. Phys. **A533**, 712 (1991); P. Danielewicz, Phys. Rev. C **51**, 716 (1995).

[35] G. Wang *et al.*, Phys. Lett. B **393**, 290 (1997).

[36] G. Wang *et al.*, Phys. Rev. C **57**, R2786 (1998).

[37] K. Kwiatkowski *et al.*, Nucl. Instrum. Methods Phys. Res. A **360**, 571 (1995).

[38] R. E. L. Green, R. G. Korteling, and K. P. Jackson, Phys. Rev. C **29**, 1806 (1984).

[39] N. T. Porile *et al.*, Phys. Rev. C **39**, 1914 (1989).

[40] T. Glasmacher *et al.*, Phys. Rev. C **50**, 952 (1994).

[41] V. Lips *et al.*, Phys. Lett. B **338**, 141 (1994).

[42] Y. Yariv and Z. Fraenkel, Phys. Rev. C **20**, 2227 (1979); **24**, 488 (1981).

[43] K. Kwiatkowski, W. A. Friedman, L. W. Woo, V. E. Viola, E. C. Pollacco, C. Volant, and S. J. Yennello, Phys. Rev. C **49**, 1516 (1994).

[44] W. D. Myers and W. J. Swiatecki, Nucl. Phys. **A587**, 92 (1995).

[45] D. Durand, Nucl. Phys. **A541**, 266 (1992).

[46] O. Lopez *et al.*, Phys. Lett. B **315**, 34 (1993).

[47] J. Cugnon, T. Mizutani, and J. Vandermuelen, Nucl. Phys. **A352**, 505 (1981).

[48] J. B. Cumming, J. Hudis, A. M. Poskanzer, and S. Kaufman, Phys. Rev. **134**, B167 (1964); J. B. Cumming, S. Katcoff, N. T. Porile, S. Tanaka, and A. Wyttenback, *ibid.* **134**, B1262 (1964).

[49] A. M. Poskanzer, G. W. Butler, and E. K. Hyde, Phys. Rev. C **3**, 882 (1971); **4**, 1759 (1971); G. D. Westfall, R. G. Sextro, A. M. Poskanzer, A. M. Zebelman, G. W. Butler, and E. Hyde, *ibid.* **17**, 1368 (1978); A. I. Warwidk, H. H. Wieman, H. H. Gutbrod, M. R. Maier, J. Petér, H. G. Pitter, H. Stelzer, and F. Welk, *ibid.* **27**, 1083 (1983).

[50] S. J. Yennello *et al.*, Phys. Rev. Lett. **67**, 671 (1991).

[51] D. S. Bracken, Ph.D. thesis, Indiana University, 1996 (unpublished).

[52] S. Yu. Shmakov *et al.*, Yad. Fiz. **58**, 1735 (1995) [Phys. At. Nucl. **58**, 1635 (1995)].

[53] L. D. Landau and E. M. Lifshitz, *Statistical Physics, Part 1* (Pergamon, New York, 1980).

[54] I. Mishustin (unpublished).